


## RESEARCH ARTICLE

# Characterization of a transitionally occupied state and thermal unfolding of domain 1.1 of $\sigma^A$ factor of RNA polymerase from *Bacillus subtilis*

Dávid Tužinčín<sup>1,2</sup> | Petr Padrta<sup>2</sup> | Hana Šanderová<sup>3</sup> | Alžběta Rabatinová<sup>3</sup> |  
Kateřina Bendová<sup>1,2</sup> | Libor Krásný<sup>3</sup> | Lukáš Žídek<sup>1,2</sup> | Pavel Kadeřávek<sup>2</sup> 

<sup>1</sup>National Centre for Biomolecular Research (NCBR), Faculty of Science, Masaryk University, Brno, Czech Republic

<sup>2</sup>Central European Institute of Technology (CEITEC), Masaryk University, Brno, Czech Republic

<sup>3</sup>Laboratory of Microbial Genetics and Gene Expression, Institute of Microbiology, Czech Academy of Sciences, Prague, Czech Republic

## Correspondence

Pavel Kadeřávek, Central European Institute of Technology (CEITEC), Masaryk University, Kamenice 5, 62500 Brno, Czech Republic.  
Email: [pavel.kaderavek@mail.muni.cz](mailto:pavel.kaderavek@mail.muni.cz)

## Funding information

Czech Science Foundation, Grant/Award Numbers: 22-12023S, GJ18-04197Y; Ministry of Education, Youth and Sports of the Czech Republic, Grant/Award Number: CZ.02.2.69/0.0/0.0/18 070/0009846; European Union, Grant/Award Number: LX22NPO5103

## Abstract

$\sigma$  factors are essential parts of bacterial RNA polymerase (RNAP) as they allow to recognize promotor sequences and initiate transcription. Domain 1.1 of vegetative  $\sigma$  factors occupies the primary channel of RNAP and also prevents binding of the  $\sigma$  factor to promoter DNA alone. Here, we show that domain 1.1 of *Bacillus subtilis*  $\sigma^A$  exists in more structurally distinct variants in dynamic equilibrium. The major conformation at room temperature is represented by a previously reported well-folded structure solved by nuclear magnetic resonance (NMR), but 4% of the protein molecules are present in a less thermodynamically favorable state. We show that this population increases with temperature and we predict its significant elevation at higher but still biologically relevant temperatures. We characterized the minor state of the domain 1.1 using specialized methods of NMR. We found that, in contrast to the major state, the detected minor state is partially unfolded. Its propensity to form secondary structure elements is especially decreased for the first and third  $\alpha$  helices, while the second  $\alpha$  helix and  $\beta$  strand close to the C-terminus are more stable. We also analyzed thermal unfolding of the domain 1.1 and performed functional experiments with full length  $\sigma^A$  and its shortened version lacking domain 1.1 ( $\sigma^{A-\Delta 1.1}$ ). The results revealed that while full length  $\sigma^A$  increases transcription activity of RNAP with increasing temperature, transcription with  $\sigma^{A-\Delta 1.1}$  remains constant. In summary, this study reveals conformational dynamics of domain 1.1 and provides a basis for studies of its interaction with RNAP and effects on transcription regulation.

## KEYWORDS

$\sigma^A$  factor, RNA polymerase, *Bacillus subtilis*, NMR, conformational exchange

## 1 | INTRODUCTION

Transcription of DNA into RNA performed by RNA polymerase (RNAP) is a key process in any living organism. Unlike in eukaryotes,

there is only a single type of RNAP in bacteria. It is an enzyme composed of several subunits. The RNAP core present in Gram-negative bacteria is composed by five subunit ( $2\alpha$ ,  $\beta$ ,  $\beta'$ ,  $\omega$ ) and two additional subunits  $\delta$  and  $\epsilon$  were identified in Gram-positive bacteria.<sup>1</sup>

This is an open access article under the terms of the [Creative Commons Attribution](https://creativecommons.org/licenses/by/4.0/) License, which permits use, distribution and reproduction in any medium, provided the original work is properly cited.

© 2023 The Authors. *Proteins: Structure, Function, and Bioinformatics* published by Wiley Periodicals LLC.

The RNAP core alone is able to elongate the transcription, but it is not capable of its initiation without a  $\sigma$  factor. The  $\sigma$  factors are essential for recognition of the promoter sequence, subsequent binding of RNAP to a promoter DNA, and beginning of the transcription process.<sup>2</sup> The recognized crucial role of  $\sigma$  subunits in the transcription process was used to develop new antibacterial drugs.<sup>3</sup>

The numbers of different  $\sigma$  factors are different in various species. There are species with only a single  $\sigma$  factor, but also with more than 100 different  $\sigma$  factors.<sup>4</sup> The  $\sigma$  factors are divided according to their structure into groups  $\sigma^{70}$  and  $\sigma^{54}$ . There are no sequential similarities between these two groups and there is also another significant difference between these two families. The factors from the  $\sigma^{54}$  family require binding ATP activators<sup>5</sup> in contrast to  $\sigma^{70}$  factors. The  $\sigma^{70}$  factors are present in all bacterial species and they are divided into four groups according to their domain composition. Vegetative  $\sigma$  factors essential for transcription of housekeeping genes are classified into group 1 ( $\sigma^{70}$  in *Escherichia coli*,  $\sigma^A$  in *Bacillus subtilis*). Groups 2–4 contain  $\sigma$  factors dedicated to transcriptions of genes expressed upon an environmental stress.<sup>4,5</sup>

The  $\sigma$  factors of the group 1 are composed of four domains: domain 1.1, domain 2 (regions 1.2–2.4), domain 3 (regions 3.0–3.2), and domain 4 (regions 4.1–4.2). Regions 2.4 and 4.2 are critical for both formation of closed complex, i.e., the initial stage of binding of RNAP to DNA, and for formation of the transcription bubble called open complex, because they are recognizing –10 and –35 promoter consensus hexamers. Region 1.2 affects the stability of the transcription bubble by an interaction with DNA between the transcription start site (+1) and the –10 hexamer. Domain 3 binds to the –10 extended motif (TGx) preceding the –10 hexamer in some promoters and serves to increase the affinity of RNAP to promoter resulting in enhancement of transcription.<sup>4</sup>

Domain 1.1 exhibits a specific autoregulation function as it inhibits the binding of the  $\sigma$  factor to DNA alone. Domain 1.1 of  $\sigma^A$  bound to free RNAP occupies the DNA binding channel.<sup>6,7</sup> The structure of domain 1.1 from *B. subtilis* consists of three  $\alpha$  helices forming a hydrophobic core and of two short  $\beta$  strands arranged in a parallel  $\beta$  sheet.<sup>8</sup> The secondary structure composition is similar to previously studied domain 1.1 from *Thermotoga maritima*.<sup>9</sup> However, the structures of these two domains differ despite the sequence similarities. The first helix in the sequences has a significantly different orientation in these two structures. Surprisingly, the arrangement of the helices forming the hydrophobic core of the domain 1.1 from *B. subtilis* is similar to domain 1.1 from *Escherichia coli*<sup>6</sup> solved by X-ray crystallography in complex with RNAP and to the structured domain of RNAP  $\delta$  subunit from *B. subtilis*.<sup>10</sup> The structure of domain 1.1 from *B. subtilis* was shown to be affected by dynamics at the  $\mu$ s–ms timescale, typical for larger structure rearrangement.<sup>8</sup> It was hypothesized<sup>8</sup> that the determined structure of the domain 1.1 from *B. subtilis* is in an exchange with a structure similar to domain 1.1 from *T. maritima*. Therefore, we decided to obtain detailed information about the low populated state of the *B. subtilis* with atomistic resolution. The results presented here then reveal details of the dynamic equilibrium between the two states, its dependence on temperature, and biological implications.

## 2 | RESULTS AND DISCUSSION

### 2.1 | Characterization of $\sigma^{1.1}$ conformational exchange

Our first goal was to determine the quantitative parameters of the previously reported exchange in the backbone of the *B. subtilis*  $\sigma^{1.1}$  domain.<sup>8</sup> We analyzed data provided by NMR experiments based on the Carr, Purcell, Meiboom and Gill pulse sequence (CPMG experiments).<sup>11,12</sup> Using the CPMG approach, we measured how exchange between conformational states contributes to the relaxation of the signal corresponding to the magnetization of <sup>15</sup>N in the protein backbone. The experiments were performed at five temperatures ranging from 10°C to 30°C. The exchange contribution to the relaxation rate at higher temperatures resulted in a significant attenuation of the NMR signal, preventing a detailed analysis of the CPMG data. At 25°C, we detected exchange increasing the relaxation rates by at least 2.5 s<sup>-1</sup> for 47 out of 71 analyzed amide <sup>15</sup>N signals. Results are summarized in Table S1. The simplest two state model of the exchange reproduced the data well. The results of the analysis of the CPMG data of individual residues show similar values of kinetic and thermodynamic parameters suggesting that they report the same exchange event. In order to test this hypothesis, we tried to fit the available data of residues exhibiting the significant exchange together to obtain a single value of the exchange contribution  $k_{ex}$  and of the population of the minor state  $p_B$  for all residues at each temperature (Table 1). The population of the minor state ranged from approximately 8% at 30°C to less than 1.0% at the lowest temperature. We should note that an increased  $\chi^2$  parameter was also observed at 30°C and in addition, we detected two residues (A35 and F54) which cannot be included in the global fit at 30°C, in contrast to the lower temperatures. It indicates that the dynamics is becoming more complicated and the application of two-state model may not be applicable at higher temperatures. Such a trend is expected because higher temperatures usually enhance population of additional states which can be safely neglected at lower temperatures. However, the significant drop of quality of NMR spectra at higher temperatures did not allow us to study the dynamics beyond the two-state model.

Despite the mentioned limitations, the determined populations follow the Boltzmann's law at the temperatures 10–25°C. We

**TABLE 1** Comparison of the fitted global exchange parameters at different temperatures to the dispersion profiles, the error represents the 99% confidence level estimated from Monte-Carlo simulations.

T(°C)	$k_{ex}$ (10 <sup>3</sup> s <sup>-1</sup> )	$p_B$ (%)	Reduced $\chi^2$
30	1.24 ± 0.01	8.2 ± 0.1	2.7
25	1.05 ± 0.02	3.87 ± 0.04	1.8
20	0.91 ± 0.01	2.18 ± 0.02	2.0
15	0.81 ± 0.02	1.30 ± 0.02	3.7
10	0.76 ± 0.04	0.78 ± 0.02	3.3

determined the enthalpy  $\Delta H = (79 \pm 5) \text{ kJ mol}^{-1}$  and entropy  $\Delta S = (0.24 \pm 0.02) \text{ kJ K}^{-1} \text{ mol}^{-1}$  differences between the major and minor state from the temperature dependence of the equilibrium constant  $K_a$  (Figure 1A). In addition to the  $K_a$  determined based on fundamental thermodynamics, we calculated also the thermodynamic parameters for reaching the transition saddle point on the free

energy landscape from the major ( $\Delta H_{AB} = (90 \pm 8) \text{ kJ mol}^{-1}$ ,  $\Delta S_{AB} = (0.09 \pm 0.03) \text{ kJ K}^{-1} \text{ mol}^{-1}$ ) and minor state ( $\Delta H_{BA} = (14 \pm 3) \text{ kJ mol}^{-1}$ ,  $\Delta S_{BA} = (-0.14 \pm 0.01) \text{ kJ K}^{-1} \text{ mol}^{-1}$ ) from the temperature dependence of the forward and backward rate constants (Figure 1B,C) (the calculated values should be interpreted with consideration of the limitations of the used Eyring equation). Extrapolation of the data to higher temperatures revealed that the low populated state accounted for ca. 12% and 20% at 37.0°C and 43.5°C, respectively.

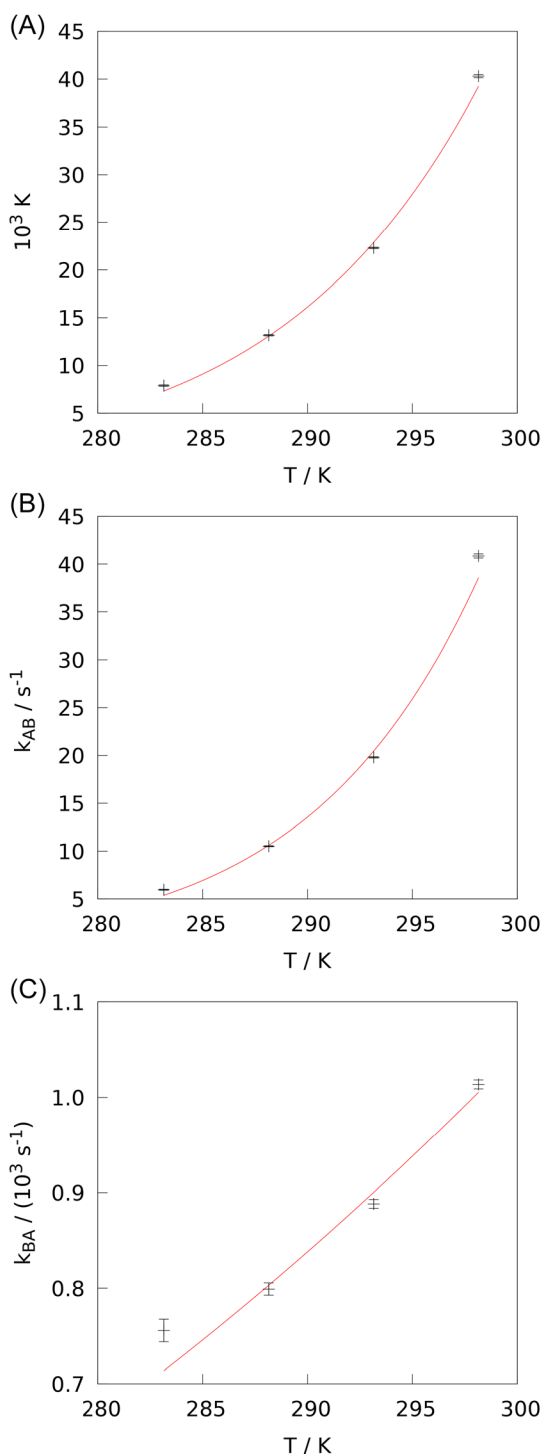


**FIGURE 1** The dependence of equilibrium constant  $K_a$  (A), forward  $k_{AB}$  (B), and backward  $k_{BA}$  (C) rate constants on temperature.

## 2.2 | Structural analysis of the minor state

The NMR structure determination of proteins is most typically based on inter-atomic proton-proton distances estimated from measured nuclear Overhauser effect (NOE).<sup>13</sup> As supplementary structural information, chemical shifts of backbone nuclei and occasionally scalar couplings or residual dipolar couplings (RDCs)<sup>14</sup> are used. Unfortunately, the portfolio of available methods for structure determination of low populated states of proteins in an exchange with their major state is more limited. It lacks the most fruitful source of structural information, that is, the inter-atomic distance. Therefore, structural analysis of minor states relies mostly on the chemical shifts and RDCs.

Chemical shifts depend on the local electronic environment of individual nuclei and therefore provide atom-specific structural information. The chemical shifts of minor protein states with populations of a few percent and (sub)millisecond exchange times are not observed directly in NMR spectra.<sup>15,16</sup> Despite that, NMR spectra of these states can be reconstructed from resonance frequencies of the major state, and chemical shift differences between states derived from CPMG experiments and/or chemical exchange saturation transfer (CEST) measurements (see Section 3). The detected changes of chemical shifts may be used to map the effects of the exchange on the structure.

Using CPMG and CEST experiments for different nuclei, we were able to obtain nearly complete  $^{15}\text{N}$ ,  $^{13}\text{C}^\alpha$ ,  $^{13}\text{CO}$ ,  $^1\text{HN}$  backbone chemical shifts (Table S2, obtained chemical shifts were deposited in the BioMagResBank <http://www.bmrb.wisc.edu><sup>17</sup> under accession code 51959), as well as  $|\Delta\omega|$  (difference between chemical shifts of major and minor state) of  $^{13}\text{C}$  methyl side-chain chemical shifts (Table S3, examples of CPMG and CEST profiles are shown in Figures S1, S2 and S3). We then combined the chemical shift changes of backbone nuclei to a single parameter  $\Delta\omega_{\text{CSP}}$ , referred to as the chemical shift perturbation (Equation (5) in Section 3).

Figure 2 shows a structure of the major conformation of  $\sigma^{1.1}$  color-coded according to the values of  $\Delta\omega_{\text{CSP}}$  for residues with the chemical shift changes evaluated for all four backbone nuclei (residues 11–65). The negligible chemical shift perturbation of flexible termini documents a similar distribution of conformations in both states of the  $\sigma^{1.1}$  domain. Therefore, we assume that the termini retain their conformational behavior. The highest  $\Delta\omega_{\text{CSP}}$  values were obtained for the residues 18, 20, 28, 31, 32, 47, 52, 56, and 65 suggesting that

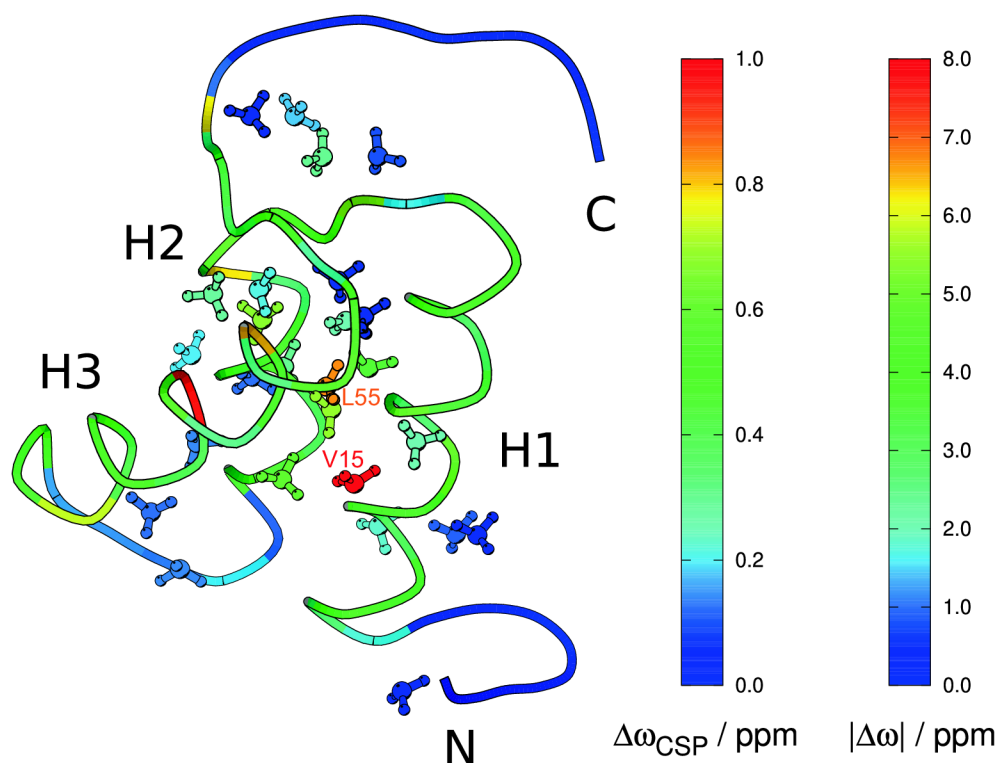


**FIGURE 2** The structure of the major state of  $\sigma^{1.1}$  (PDB 5MWW) color coded according to the size of backbone  $\Delta\omega_{\text{CSP}}$  (colored backbone) and methyl  $|\Delta\omega|$  (colored models of  $\text{CH}_3$  groups) determined for the minor state. The red and orange  $\text{CH}_3$  models correspond to pro-S methyl of V15 and pro-R methyl of L55, respectively.

these residues are in a much different local environment in the minor vs. major state.

Positions of the methyl groups are also depicted in Figure 2 and color-coded according to  $|\Delta\omega|$ . In proteins, methyl groups are sensitive indicators of structure and dynamics<sup>18</sup> and they often report on events within the hydrophobic core. The CPMG experiments measured with  $\sigma^{1.1}$  samples including stereospecifically labeled methyl groups provided us a complete set of  $^{13}\text{C}$  methyl chemical shifts of the minor state. The most significant changes were identified for  $^{13}\text{C}^{\gamma}$ -proS of V15,  $^{13}\text{C}^{\delta}$ -proS of L19, both methyls in I34, and  $^{13}\text{C}^{\delta}$ -proR of L55. All these methyls are located in a proximity of aromatic rings in the major state ( $^{13}\text{C}^{\gamma}$ -proS of V15 is close to F41, other mentioned methyls are in the proximity of Y51). It can be expected that the significant disturbance of their chemical shifts is induced by a change of the distance and orientation to the aromatic rings, known for a strong effect on the chemical shifts.<sup>19</sup> Generally, the results indicate a larger structural rearrangement affecting the hydrophobic core of the  $\sigma^{1.1}$  structure.

### 2.3 | Partial disorder of the minor state

The backbone chemical shift are very sensitive to the secondary structures. A lower dispersion of backbone amide proton chemical shifts (Figure S4) indicates lower tendency of the minor state to form secondary structures. Comparison of chemical shifts of all backbone nuclei with their random-coil values (Figure S5) confirmed that the chemical shift changes can be interpreted as a consequence of lower propensity of the minor state to form secondary structure.

Backbone chemical shifts also allowed us to predict the order parameters  $S^2$ , measuring angular amplitudes of motion for the backbone amide groups. The values estimated by the RCI approach,<sup>20</sup> plotted in Figure 3, were lower for the minor state, in agreement with the lower content of secondary structures. The  $S^2$  values indicate that the minor state exhibits higher flexibility (compared to the major state) in the regions corresponding to helix 1 (residues F12–R26), helix 3 (residues S45–E57) and  $\beta$ -sheet 1 (residues V28–T30). The N-termini (amino acids A1–T11) and the C-termini (amino acids S64–D71) remain flexible in both states.

In order to quantify the tendency to form the secondary structures, the parameter secondary structure propensity (SSP)<sup>21</sup> was calculated from chemical shifts<sup>22</sup> of both states. SSP combines chemical shifts from different nuclei (in this case, all the aforementioned backbone nuclei) into a single score representing the expected tendency of a residue to form  $\alpha$ -helical (positive value) or extended structure (negative value). The results are presented in Figure 4. Compared to the SSP of the major state, overall decrease in propensity to form secondary structure is observed across all structural elements of the minor state. However, SSP is not uniform in the minor state. The strongest tendency to form secondary structures was observed for helix 2 and for the  $\beta$ -sheet. The minor state deviates from a random coil conformation more than typical intrinsically disordered proteins (several examples are presented in Figure S6). Most likely, the minor state can be characterized as an ensemble of rapidly inter-converting substates (not resolved on the  $\mu\text{s}$ – $\text{ms}$  time scale probed by our experiments). The ensemble is dominated by conformation with a folded central region, consisting of helix 2 and the adjacent  $\beta$ -sheet. This conclusion is supported by RDCs measured for both states as shown in



**FIGURE 3** Dependence of the estimated order parameter  $S^2$  based on RCI approach calculated for the major (blue) and minor (red) states of  $\sigma^{1.1}$ .

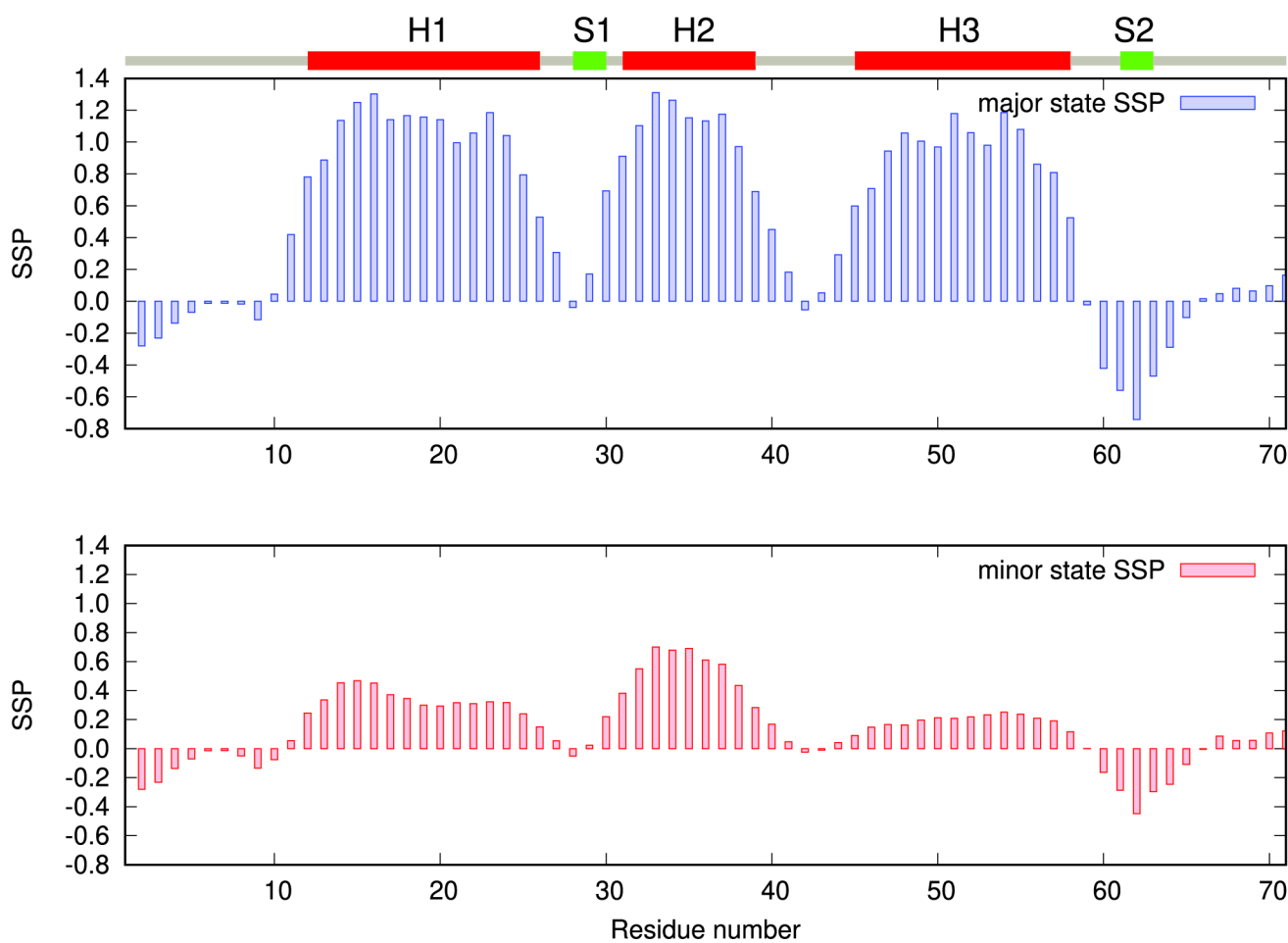
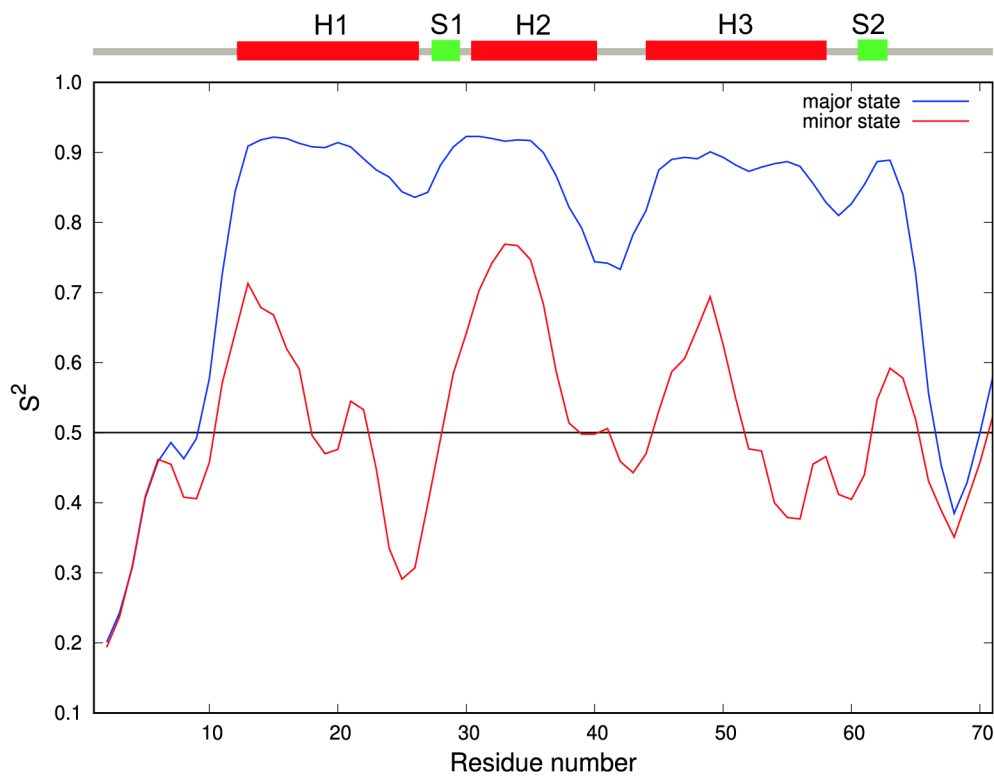


**FIGURE 4** Secondary structure propensity prediction calculated for major state (top, blue), and minor state (bottom, red). Secondary structures of major state are shown above the graph, helical structures are in red, beta sheets structures are in green.

Figures S7 and S8. Whereas RDCs determined for the major state are in a good agreement with the previously solved structure,<sup>8</sup> RDCs of the minor state are more scattered, suggesting that the native structure is not retained.

Our investigation of the low populated state of the domain 1.1 is one of a very limited number of studies of excited states of proteins. Currently, NMR is the only method which allows us to determine temporarily present structures with population of few percent in a dynamic exchange with the major state. Nevertheless, NMR methods developed for this purpose<sup>23,24</sup> provide a fruitful insight into possible conformational adaptability of proteins and the minor states may represent biologically interesting transition states accessed during a ligand binding or may play a role in a binding controlled by a conformational selection. In our case, the advanced NMR methods revealed a presence of a less ordered state at a temperature far below the melting point (see below) and allowed us to describe its structural features with atomic resolution. The NMR analysis thus provided information not available at elevated temperatures due to line broadening in the NMR spectra.

## 2.4 | Exchange rates of amide protons

In addition to the characterization of the minor state we performed an experiment to monitor a proton–deuterium exchange of backbone amides of the major state at 1°C after a quick replacement of the protonated buffer for its deuterated equivalent. Decays of amide signal intensities in time were converted to protection factors (available in Figure S9). The exchange rate of residues outside the secondary structure elements were too fast to be detected by our approach. The protection factors of residues within the secondary structure elements were in the order of  $10^2$ – $10^3$  while the protection factors of structured proteins are expected to be in the orders  $10^6$ – $10^9$ .<sup>25</sup> It suggests the presence of a significantly less ordered state. The assumption that the population of the minor state at 1°C is 0.24% (based on thermodynamical parameters of the exchange process detected by relaxation dispersion experiments) allow us to estimate the protection factor of the minor state to be found in between 0.2 and 6. The value of the protection factor lower than one indicates that the relaxation dispersion experiments detected only part of the states which reduce the protection factors.

## 2.5 | Thermal unfolding of the domain 1.1

As the NMR data revealed a presence of less ordered/disordered state(s), we complemented our study by differential scanning calorimetry (DSC) and circular dichroism spectroscopy (CD) measured at multiple temperatures which allowed us to study thermal unfolding of  $\sigma^{1.1}$ . The DSC data were interpreted with a simple two-state model and a more sophisticated sequential Zimm–Bragg model.<sup>26</sup> The agreement of the calorimetry data with the two state model was poor unless the van't Hoff enthalpy is fitted separately from the overall

heat (data not shown). The Zimm–Bragg model provided a better, but not perfect agreement with the DSC data (results shown in Figure S10). The optimized Zimm–Bragg model was further cross-validated using CD data<sup>27</sup> which reflects the dependence of the helicity on the temperature. Non-negligible deviations were observed at higher temperatures (Figure S10). The content of unfolded protein at low temperatures predicted by the Zimm–Bragg model was significantly higher than the population of the minor state revealed by the NMR relaxation dispersion. Also, the Zimm–Bragg model predicted quite high reduction of the helical character (approximately 11%) of the protein at 1°C compared to the estimation of the amount of the disordered state calculated from the proton–deuterium exchange experiment. Altogether, the DSC and CD data provide additional information about the conformational behavior at high temperatures which cannot be described by simple models.

## 2.6 | Functional characterization of $\sigma^{1.1}$ in dependence on temperature

What is a possible role of the thermal unfolding of domain 1.1 in the biological function of  $\sigma^{1.1}$ ? Reversible thermal denaturation of  $\sigma^{1.1}$  domain is observed with  $T_m \approx 47^\circ\text{C}$ . However, the less structured nature of  $\sigma^{1.1}$  at high temperatures does not exclude its physiological function. Currently, intrinsically disordered proteins are fully accepted as a functional part of the proteome with unique biophysical properties allowing them to play various roles requiring high flexibility and access to a larger conformational space than occupied by rigid proteins. Notably, there is no crystal structure of RNAP with the  $\sigma^A$  subunit from *B. subtilis* available and a weak electron density map of  $\sigma^{1.1}$  in the crystal structure of RNAP from *E. coli* indicates that  $\sigma^{1.1}$  is highly mobile in the holoenzyme.<sup>7</sup> Domain 1.1 is ejected from the RNAP channel during formation of the closed complex and its electron density is no longer observable.<sup>28</sup>

To provide insights into the potential functional importance of the equilibrium between the ordered and less ordered states of  $\sigma^{1.1}$  we performed in vitro multiple round transcription experiments with two variants of  $\sigma$ . We used the *B. subtilis* RNAP core containing also  $\delta$  and  $\epsilon$  reconstituted with either full-length  $\sigma^A$  or  $\sigma^{A\Delta 1.1}$ . The latter  $\sigma$  variant lacked 71 N-terminal residues—the entire domain 1.1. Transcriptions were initiated from the strong *B. subtilis* rRNA promoter *rrnB* P1<sup>29</sup> at two temperatures, 30°C and 45°C. Figure 5 shows differential effects of the two temperatures on transcription, depending on the  $\sigma$  factor variant. Transcription with  $\sigma^{A\Delta 1.1}$  was virtually insensitive to temperature, whereas transcription with  $\sigma^A$  resulted in increased transcriptional output at the higher temperature. This result is consistent with increasing flexibility of this domain with temperature. The conformational plasticity affecting the hydrophobic core might be important for entry/exit of this domain into/from the primary channel of RNAP. From the biological point of view, it correlates with the need for increased transcriptional output at the higher temperature as *B. subtilis* cells grow at the fastest growth rate in the 45–50°C range.<sup>30</sup>

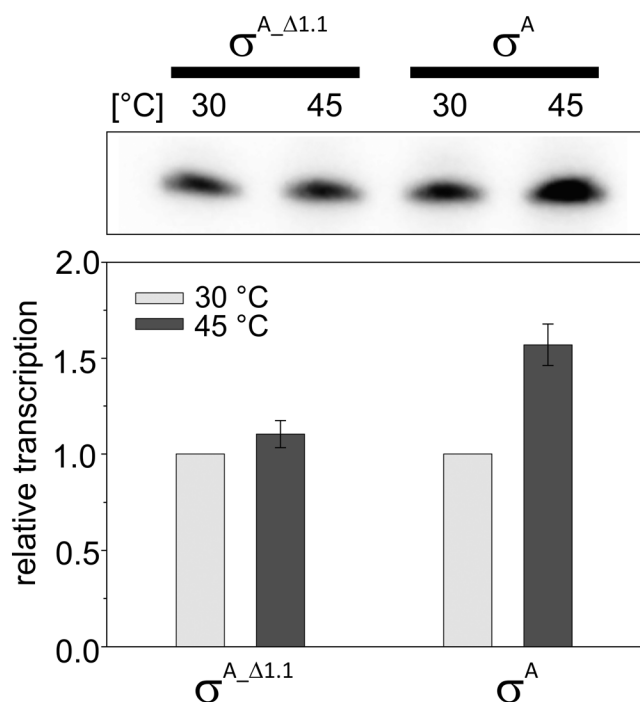


**FIGURE 5** Functional characterization of  $\sigma^{1.1}$  in dependence on temperature. Multiple round transcription were performed with RNAP reconstituted with  $\sigma^A$  or  $\sigma^{A_{\Delta 1.1}}$ . Representative primary data are shown above the graph, the bands are radiolabeled transcripts resolved on a polyacrylamide gel. The graph shows averages of three independent experiments  $\pm$  SD. To facilitate comparison of the differential effects, transcription activity at 30°C for both  $\sigma$  variants was set as 1.

Interestingly,  $\sigma^{1.1}$  of Mycobacteria like *M. smegmatis*<sup>31</sup> or *M. tuberculosis* (Figure S11) are predicted to be disordered which further supports the hypothesis of the biological relevance of the disordered states of the  $\sigma^{1.1}$  from *B. subtilis*. It suggests that this conformational plasticity affecting the hydrophobic core is important for entry/exit of this domain into/from the primary channel of RNAP. This hypothesis is consistent with a recent study that investigated effects of the point mutation I48S in  $\sigma^{70}$  on transcription in *E. coli*,<sup>32</sup> where a disturbance of the hydrophobic core of the protein resulted in significant phenotypic changes compared to the wild-type. Although the mutated residue I48 is weakly conserved in primary  $\sigma$  factors, it is often replaced with leucine or valine with similar biophysical properties. In *B. subtilis* this position corresponds to L55, which is located in the C-terminal  $\alpha$  helix and its sidechain was shown in our study to be highly affected by the conformational exchange (Figure 2 and Table S3). A parallel can be found also with the  $\omega$  subunit of RNAP, where its flexibility is essential for its function, and even silent mutations (mutations that do not change amino acids but codons; subsequently, due to differential availability of aminoacylated tRNAs, the protein is folded differently) that reduce this flexibility compromise its interplay with RNAP and its biological function.<sup>33</sup>

The higher tendency of the minor state to form  $\alpha$  helix 2 and the  $\beta$ -sheet suggests that these secondary structure elements represent a

core of the  $\sigma^{1.1}$  structure. Interestingly, the less ordered helices 1 and 3 interact in *E. coli* RNAP holoenzyme with an  $\alpha$  helix in a linker between domains 1.1. and 1.2, and with the Gp2 inhibitor produced by the bacteriophage T7.<sup>6</sup> Helices 1 and 3 are oriented towards to the  $\beta'$  clamp whose motion was proposed to eject  $\sigma^{1.1}$  from the RNAP cleft.<sup>28</sup>

## 2.7 | Conclusions

We characterized a previously detected low populated state of the  $\sigma^{1.1}$  domain from RNA polymerase of *Bacillus subtilis*. Its population is about 4% at 25°C undergoing an exchange with the major state at the rate of approximately  $10^3 \text{ s}^{-1}$ . The determined thermodynamic parameters predict an increase of the population of the minor state with the increasing temperature, reaching 20% at 43.5°C. The previously suggested hypothesis<sup>8</sup> that the excited state of the  $\sigma^{1.1}$  domain from *B. subtilis* is similar to another known structure of  $\sigma^{1.1}$  domain from *T. maritima* appears to be incorrect. Instead, the studied minor state was identified to be more flexible than the major state and it has a lower propensity to form a structured conformation, especially for helices 1 and 3. We have shown that the disorder induced by the elevated temperature increases the transcriptional output. We hypothesize that the conformational plasticity of  $\sigma^{1.1}$  plays a role in binding and ejection of the domain 1.1 from the binding channel of RNAP.

## 3 | MATERIALS AND METHODS

### 3.1 | Sample preparation

Cloning procedure of gene encoding  $\sigma^{1.1}$  was described elsewhere.<sup>8</sup> Expression and purification of samples are described in Appendix S1. A purity and stability of the samples was verified prior to every NMR measurement. A special attention was paid to avoid a contamination of glycerol which increases viscosity of the solvent and affects the measured relaxation rates. Four samples of wild-type  $\sigma^{1.1}$  were prepared in this study, each differing in the isotopic labeling scheme, while the buffer composition was the same, the samples contained 20 mM sodium phosphate buffer, 10 mM NaCl, 3 mM  $\text{NaN}_3$ , and the pH was 6.6. The first sample of 1 mM concentration was uniformly labeled with  $^{15}\text{N}$ ,  $^{13}\text{C}$  in a protonated solvent. The second sample of 0.8 mM concentration was uniformly labeled with  $^{15}\text{N}$  and contained  $^1\text{H}$  at all exchangeable positions, in addition,  $^{13}\text{C}$  and  $^1\text{H}$  were incorporated into methyl groups of Thr, Met and pro-S Leu, Ile and Val residues.<sup>34</sup> All other positions contained  $^2\text{H}$  and  $^{12}\text{C}$ . The third sample of 0.4 mM concentration was prepared in the same way as the second one, with the exception of  $^{13}\text{C}$  and  $^1\text{H}$  being incorporated in different methyl groups of Ala and pro-R Leu, Ile and Val residues.<sup>35</sup> The fourth sample of 0.8 mM concentration contained  $^2\text{H}$  at all exchangeable positions and was labeled selectively at the  $^{13}\text{C}^\alpha$  positions with the exception of Ile, Leu, and Val, where  $^{13}\text{C}^\alpha$  was partially enriched.<sup>36</sup> All other positions contained natural abundance of  $^1\text{H}$  and  $^{12}\text{C}$ .

### 3.2 | CPMG/CEST measurements

All NMR experiments were performed using Bruker Avance Neo spectrometers. The  $^{15}\text{N}$  single-quantum relaxation dispersion experiments were performed on  $^{13}\text{C}$ ,  $^{15}\text{N}$  uniformly labeled sample at 10°C, 15°C, 20°C, 25°C, and 30°C using NMR spectrometers operating at proton frequencies of 600 and 850 MHz, equipped with cryogenically cooled TCI probes. The  $^{15}\text{N}$  CPMG experiment was performed in a relaxation compensated version,<sup>37</sup> with optimized phase cycles applied to  $^{15}\text{N}$  CPMG refocusing pulses.<sup>38</sup> Backbone amide  $^{15}\text{N}$ - $^1\text{H}$  residual dipolar couplings of the minor conformation were obtained by measuring a set of CPMG relaxation dispersion experiments (TROSY, anti-TROSY and  $^1\text{H}$  continuous wave decoupled CPMG<sup>39</sup>) on partially aligned samples at 25°C at 600 MHz (equipped with a cryogenically cooled TCI probe), 700 MHz (equipped with a cryogenically cooled TXO probe), and 850 MHz (equipped with a cryogenically cooled TCI probe). The maximum CPMG frequency was 1 kHz and the CPMG relaxation delay was set to 36 ms in all  $^{15}\text{N}$  CPMG experiments. Alignment was achieved using Pf1 phage<sup>40</sup> (approximately 18 mg/mL, ASLA Biotech) and PEG (C12E5)/hexanol media.<sup>41</sup> The analysis of CPMG experiments measured with alignment media were complemented with experiments for measurement of the amide  $^{15}\text{N}$  longitudinal relaxation rates and relaxation rates of two-spin order<sup>39</sup> of the amide  $^{15}\text{N}$ - $^1\text{H}$  spin pair. Residual dipolar couplings of the major state conformation were measured using the IPAP approach.<sup>42</sup>  $^{15}\text{N}$  chemical shifts of the minor state were verified by a CEST experiment<sup>43</sup> performed at a 950 MHz spectrometer equipped with a cryogenically cooled TCI probe using  $^{15}\text{N}$  labeled NMR sample. The CEST experiment was measured with the relaxation delay  $T_{\text{EX}} = 0.4$  s and irradiation with  $^{15}\text{N}$   $B_1$  field amplitude 29 Hz. The  $^{15}\text{N}$  carrier frequency was set to 118.5 ppm and the CEST irradiation offset ranged from -1800 to 1650 Hz with 25 Hz steps. Values of  $^{13}\text{C}^\alpha$ ,  $^{13}\text{CO}$ ,  $^1\text{HN}$  chemical shifts of the minor state have been derived from CEST-based experiments.<sup>44-47</sup> The  $^{13}\text{CO}$  CEST experiment<sup>46</sup> was performed at the 700 MHz spectrometer equipped with a cryogenically cooled TXO probe with the  $^{13}\text{C}$  and  $^{15}\text{N}$  uniformly labeled sample, the CEST irradiation with the  $B_1$  field amplitude 32 Hz was applied during the  $T_{\text{EX}} = 0.4$  s period. The  $^{13}\text{C}$  carrier was set to 178.7 ppm and the CEST irradiation offsets ranged from -1400 to 1400 Hz with spacing of 25 Hz. The  $^{13}\text{C}^\alpha$  CEST experiment<sup>44</sup> was performed at the 700 MHz spectrometer equipped with a cryogenically cooled TXO probe with the specifically labeled  $^{13}\text{C}^\alpha$  sample and at the 700 MHz spectrometer equipped with a cryogenically cooled TCI probe with uniformly  $^{15}\text{N}$  and  $^{13}\text{C}$  labeled sample using a different variant of the CEST experiment<sup>45</sup> with detection in the form of  $^1\text{H}$ - $^{15}\text{N}$  correlation spectra. The identical length of the CEST irradiation period  $T_{\text{EX}} = 0.4$  s was used in all  $^{13}\text{C}^\alpha$  CEST experiments together with the CEST irradiation offsets ranging from -2050 to 2100 Hz with 50 Hz spacing. The CEST experiment performed with the specifically labeled sample was measured with the CEST  $^{13}\text{C}$   $B_1$  irradiation field amplitude 26 Hz, the  $^{13}\text{C}$  carrier frequency was set to 57 ppm. The  $^{13}\text{C}^\alpha$  CEST experiment measured with the uniformly labeled sample was performed with the CEST  $^{13}\text{C}$   $B_1$  field of 30 Hz and the  $^{13}\text{C}$  carrier frequency was set to 58 ppm.

The same experiment was repeated with the setup adjusted for glycine residues with the CEST  $^{13}\text{C}$   $B_1$  field amplitude 31 Hz, the  $^{13}\text{C}$  carrier frequency set to 43.4 ppm and the CEST irradiation  $^{13}\text{C}$  offsets ranging from -1250 to 1600 Hz with spacing of 25 Hz. The amide proton chemical shifts were determined based on CEST experiments measured using selective pulse excitation<sup>47</sup> of sweep width 1200 and 1250 Hz and with 3 excitation elements in the used waveform. All measurements of proton CEST were carried out on the 850 MHz spectrometer with the proton carrier frequency set to the water frequency (4.7 ppm) and the CEST irradiation of the length  $T_{\text{EX}} = 0.8$  s with offsets ranging from 2605 to 3855 Hz with 25 Hz step. The first proton CEST experiment with the amplitude of the CEST irradiation 29 Hz was performed with the deuterated sample containing specifically labeled methyl positions at Thr, Met and pro-S Leu, Ile and Val residues. The second experiment was performed with the  $B_1$  field amplitude 25 Hz using the uniformly  $^{15}\text{N}$  labeled sample to improve the analysis for residues which signal intensities in the  $^1\text{H}$ - $^{15}\text{N}$  correlation spectra were attenuated in the previous experiment due to the specific labeling. Methyl relaxation dispersion experiments were performed with samples specifically labeled at methyl positions using the Pf1 phage as an alignment medium<sup>40</sup> (approximately 18 mg/mL, ASLA Biotech). The spin state selective and  $^1\text{H}$  continuous wave decoupled CPMG experiments<sup>48</sup> were run at the 850 MHz (equipped with a cryogenically cooled TCI probe) and 700 MHz (equipped with a cryogenically cooled TXO probe) NMR spectrometers with the relaxation delay 30 ms and maximum CPMG frequency 1500 Hz. The sign of the change of the methyl chemical shift was estimated by a comparison of HSQC and HMQC spectra.<sup>49</sup>

### 3.3 | H/D exchange

The 1 mM  $^{15}\text{N}$  labeled sample in the same buffer composition as described above was loaded on a desalting column filled with a deuterated buffer of the otherwise identical composition. The collected protein which passed the column was quickly transferred to the 600 MHz spectrometer (equipped with a cryogenically cooled TCI probe) and after adjustment of the proton coil tuning and homogeneity of the magnetic field a series of  $^1\text{H}$ - $^{15}\text{N}$  BEST-HSQC was started. The delay between the loading of the sample to desalting column and beginning of the first experiment was 7.6 min. We collected 93 increments in indirect dimension in each spectra resulting in one spectra acquisition in approximately 5 min. The stability of the NMR system was checked regularly during the measurement by a detection of signals of aliphatic protons in one-dimensional proton spectrum with water suppression.

### 3.4 | Differential scanning calorimetry

The DSC thermograms of  $\sigma^{1.1}$  were collected on a Microcal PEAQ-DSC Automated (Malvern) instrument. The concentration of protein was 0.75 mg/mL in a phosphate buffer identical to the NMR buffer



(20 mM NaPi, 10 mM NaCl, 3 mM NaN<sub>3</sub>, pH 6.6). Triplicate measurement was performed. Both buffer and sample solutions were degassed before measurements. The following measurement parameters were used: the temperature scan range was 4–85°C, scan heat rate was 60°C/h, pre-scan thermostat was set to 5 min, post-scan thermostat was 0 min, feedback mode was set to high. Evaluation of the DSC data was performed using MicroCal PEAQ-DSC software (Malvern).

### 3.5 | Circular dichroism spectroscopy

Circular dichroism (CD) spectra of  $\sigma^{1.1}$  were measured using Jasco J-815 CD spectrometer. The concentration of protein was 0.1 mg/mL in a phosphate buffer identical to the NMR buffer (20 mM NaPi, 10 mM NaCl, 3 mM NaN<sub>3</sub>, pH = 6.6). Experiments were performed in a quartz glass cell with a 0.1 cm path length. Spectra (200–260 nm) were recorded in the range of 5–90°C in 5°C temperature steps. Each spectrum was recorded with total of three scans.

### 3.6 | Data analysis

Data acquired from NMR measurements were converted and processed using the software NMRPipe,<sup>50</sup> non-uniformly sampled data were processed using NMRPipe, version 9.9, and SMILE 2.0beta. No extrapolation was used in the processing of the non-uniformly sampled data and identical signal downscaling factor was used for independently processed spectra in relaxation or CEST series. The analysis and visualization of spectra were done in the software NMRFAM-Sparky.<sup>51</sup> In CPMG data sets signal intensities obtained from 2D spectra measured in relaxation series were converted into the effective relaxation rates  $R_{2,eff}$  using the Octave 3.8.2 program<sup>52</sup> employing the function `leasqr` from the package `optim`, by fitting peak intensities to a mono-exponential decay using a nonlinear least-squares approach:

$$I_1(\nu_{CPMG}) = I_0 e^{-R_{2,eff} T} \quad (1)$$

where  $\nu_{CPMG} = 1/4\tau$ , with  $2\tau$  being the interval between consecutive refocusing pulses of the CPMG sequence that is applied during a constant relaxation delay of duration  $T$ .  $I_1(\nu_{CPMG})$  and  $I_0$  are the signal intensities in spectra measured with and without the relaxation delay  $T$ . The error in peak intensities was estimated from the random spectral noise sampled at 10000 random positions, outside of peak regions. Uncertainties in the  $R_{2,eff}$  relaxation rates were determined by 2000 Monte Carlo simulation steps. Subsequently, relaxation dispersion profiles were fitted to the Carver-Richards two-site exchange model<sup>53</sup> using a software package GLOVE.<sup>54</sup> The global exchange parameters,  $p_B$  (population of the minor state) and  $k_{ex}$  (exchange rate) were extracted by global fitting. Values of  $\Delta\omega$  (chemical shift difference between the states) were extracted on the per-residue basis. Uncertainties in the exchange parameters were established by 5000 Monte Carlo simulations. The dependence of the population of the

minor state  $p_B$  on temperature was used to obtain the change of enthalpy  $\Delta H$  and entropy  $\Delta S$  upon transition to the minor state following the Boltzmann's law:

$$K_a = \frac{p_B}{1-p_B} = e^{-(\Delta H - T\Delta S)/RT}, \quad (2)$$

where  $R$  is the molar gas constant,  $T$  is the absolute temperature, and the fraction  $p_B/(1-p_B)$  represents the equilibrium constant  $K_a$ .

The change of enthalpy and entropy for a transition from the ground state ( $\Delta H_{AB}$  and  $\Delta S_{AB}$ , respectively) or from the minor state ( $\Delta H_{BA}$  and  $\Delta S_{BA}$ , respectively) to a transition saddle point was determined following the Eyring equation:

$$k_{AB} = p_B k_{ex} = \frac{k_B T}{h} e^{-(\Delta H_{AB} - T\Delta S_{AB})/RT}, \quad (3)$$

$$k_{BA} = (1-p_B) k_{ex} = \frac{k_B T}{h} e^{-(\Delta H_{BA} - T\Delta S_{BA})/RT}, \quad (4)$$

where  $k_B$  is the Boltzmann's constant,  $h$  is the Planck constant, and  $T$  is the thermodynamic temperature. Standard deviations of thermodynamic parameters were estimated using the smooth Bootstrap method.

In CEST data sets, the peak intensities were collected from 2D spectra in  $B_1$  position series. Uncertainties in intensities were estimated in the same way as mentioned above. CEST profiles were generated and exchange parameters were extracted using the software ChemEx<sup>43</sup> (<http://www.github.com/gbouvnigies/chemex>). Global/per-residue fitting as well as uncertainty estimation was done as described for the CPMG data set.

The chemical shift perturbation was calculated as

$$\Delta\omega_{CSP} = \sqrt{\frac{1}{n} \sum_i (\alpha_i \Delta\omega_i)^2}, \quad (5)$$

where  $n$  was the number of available chemical shift disturbance for backbone nuclei in each residue and the parameters  $\alpha_i$  were 0.32, 0.19, 0.12, and 1.00 for <sup>13</sup>C $\alpha$ , <sup>13</sup>C $\beta$ , <sup>15</sup>N, and <sup>1</sup>H $\alpha$  nuclei, respectively (the parameters  $\alpha_i$  were calculated from the ranges of chemical shifts of our protein of interest).

### 3.7 | $\sigma^{A-\Delta 1.1}$ cloning

The coding sequence for  $\sigma^{A-\Delta 1.1}$  (amino acids 72–371 from the *B. subtilis sigA* gene) was amplified by PCR using primers #1263 (5' cggcatggatcctaattcagcagcttgc 3') and #1195 (5' ccgctcgagtattcaaggaaatcttc 3') inserted into plasmid pET28b between NcoI and XhoI sites. The DNA fragment was cloned with the natural stop codon; the protein product did not contain any affinity tag. At the 5' of the fragment, sequence encoding Met was added (part of the NcoI cloning site). The sequence was verified by sequencing. The verified plasmid was transformed into *E. coli* expression strain BL21 (DE3) (LK1367).

### 3.8 | Protein purification

$\sigma^A$  (plasmid pCD2, LK1365) and  $\sigma^{A-\Delta 1.1}$  (LK1367) were purified using the same protocol as described in Ref. 55. *B. subtilis* RNAP (MH5636, LK1723) was purified as described in Ref. 56.

### 3.9 | In vitro transcription

RNAP was reconstituted with a  $\sigma^A$  or  $\sigma^{A-\Delta 1.1}$  (RNAP: $\sigma$  ratio = 1:10). Reconstitutions were carried out in buffer A (50 mM Tris-Cl [pH 8.0], 100 mM NaCl, 50% glycerol, 3 mM  $\beta$ -mercaptoethanol) at 30°C for 30 min. Multiple-round transcriptions were carried out in 10  $\mu$ L reaction volumes in transcription buffer containing 40 mM Tris-HCl (pH 8.0), 150 mM KCl, 10 mM MgCl<sub>2</sub>, 1 mM dithiothreitol (DTT), and 0.1 mg/ml bovine serum albumin (BSA). As a template, 0.8 nM supercoiled plasmid bearing the *rmB* P1 cloned into P770 (LK176<sup>57</sup>) was used. ATP, CTP, and GTP were 200  $\mu$ M; UTP was 10  $\mu$ M plus 2  $\mu$ M radiolabeled [ $\alpha$ -<sup>32</sup>P]UTP. The final concentration of RNAP in in vitro transcriptions was 30 nM. All transcription experiments were done at 30°C or 45°C, respectively, and transcriptions were allowed to proceed for 15 min. Transcriptions were stopped with equal volumes of formamide stop solution (95% formamide, 20 mM EDTA [pH 8.0]). Samples were loaded onto 7 M urea-6.5% polyacrylamide gels and electrophoresed. The dried gels were exposed to BAS IP MS screens. The screens were scanned with Typhoon 5 (Cytiva). The amounts of the 145-nucleotide-long transcripts (originating from the cloned promoter) were quantified with ImageQuantTL software (Cytiva). All calculations and data fitting were done using SigmaPlot from Jandel Scientific.

#### AUTHOR CONTRIBUTIONS

**Dávid Tužičin:** Investigation; writing – original draft; validation. **Petr Padrta:** Investigation. **Hana Šanderová:** Investigation. **Alžběta Rabatinová:** Investigation. **Kateřina Bendová:** Investigation. **Libor Krásný:** Writing – review and editing; conceptualization. **Lukáš Židek:** Writing – review and editing; writing – original draft; supervision; conceptualization. **Pavel Kadeřávek:** Investigation; funding acquisition; writing – review and editing; writing – original draft; supervision; project administration; conceptualization.

#### ACKNOWLEDGMENTS

This work was supported by Czech Science Foundation grant Nos. GJ18-04197Y (to Pavel Kadeřávek and Dávid Tužičin) and 22-12023S (to Lukáš Židek, Petr Padrta, Hana Šanderová, Libor Krásný), from European Regional Development Fund-Project MSCA-fellow2@MUNI (No. CZ.02.2.69/0.0/0.0/18 070/0009846). CIISB, Instruct-CZ Centre of Instruct-ERIC EU consortium, funded by MEYS CR infrastructure project LM2018127, is gratefully acknowledged for the financial support of the measurements at the Josef Dadok National NMR Centre and CF Biomolecular Interactions and

Crystallization. Libor Krásný acknowledges the project National Institute of Virology and Bacteriology (Programme EXCELES, ID Project No. LX22NPO5103)—Funded by the European Union—Next Generation EU. Authors thank Lewis Kay, Enrico Rennella, and Ranjith Muhandiram for providing NMR pulse sequences for measurement CEST and CPMG experiments and Guillaume Bouvignies for discussion of analysis of data using the software ChemEx.

#### CONFLICT OF INTEREST STATEMENT

The authors declare no conflict of interest.

#### PEER REVIEW

The peer review history for this article is available at <https://www.webofscience.com/api/gateway/wos/peer-review/10.1002/prot.26531>.

#### DATA AVAILABILITY STATEMENT

The additional data that support the findings of this study are available from the corresponding author upon reasonable request.

#### ORCID

Pavel Kadeřávek  <https://orcid.org/0000-0002-3561-354X>

#### REFERENCES

1. Weiss A, Shaw LN. Small things considered: the small accessory subunits of RNA polymerase in gram-positive bacteria. *FEMS Microbiol Rev.* 2015;39(4):541-554.
2. Murakami KS, Darst SA. Bacterial RNA polymerases: the whole story. *Curr Opin Struct Biol.* 2003;13(1):31-39.
3. Ma C, Yang X, Kandemir H, et al. Inhibitors of bacterial transcription initiation complex formation. *ACS Chem Biol.* 2013;8(9):1972-1980.
4. Paget MS. Bacterial sigma factors and anti-sigma factors: structure, function and distribution. *Biomolecules.* 2015;5(3):1245-1265.
5. Österberg S, del Peso-Santos T, Shingler V. Regulation of alternative sigma factor use. *Annu Rev Microbiol.* 2011;65:37-55.
6. Bae B, Davis E, Brown D, Campbell EA, Wigneshweraraj S, Darst SA. Phage T7 Gp2 inhibition of *Escherichia coli* RNA polymerase involves misappropriation of  $\sigma^{70}$  domain 1.1. *Proc Natl Acad Sci.* 2013;110(49):19772-19777.
7. Murakami KS. X-ray crystal structure of *Escherichia coli* RNA polymerase  $\sigma^{70}$  holoenzyme. *J Biol Chem.* 2013;288(13):9126-9134.
8. Zachrdla M, Padrta P, Rabatinová A, et al. Solution structure of domain 1.1 of the  $\sigma^A$  factor from *Bacillus subtilis* is performed for binding to the RNA polymerase core. *J Biol Chem.* 2017;292(28):11610-11617.
9. Schwartz EC, Shekhtman A, Dutta K, et al. A full-length group 1 bacterial sigma factor adopts a compact structure incompatible with DNA binding. *Chem Biol.* 2008;15(10):1091-1103.
10. Papoušková V, Kadeřávek P, Otrusínová O, et al. Structural study of the partially disordered full-length  $\delta$  subunit of RNA polymerase from *Bacillus subtilis*. *ChemBiochem.* 2013;14(14):1772-1779.
11. Purcell EM, Carr HY. Effects of diffusion on free precession in nuclear magnetic resonance experiments. *Phys Rev.* 1954;94:630-638.
12. Gill D, Meiboom S. Modified spin-echo method for measuring nuclear relaxation times. *Rev Sci Instrum.* 1958;29:688-691.

13. Wüthrich K. NMR with proteins and nucleic acids. *Europhys News*. 1986;17(1):11-13.
14. Tjandra N, Bax A. Direct measurement of distances and angles in biomolecules by NMR in a dilute liquid crystalline medium. *Science*. 1997;278(5340):1111-1114.
15. Korzhnev DM, Kay LE. Probing invisible, low-populated states of protein molecules by relaxation dispersion NMR spectroscopy: an application to protein folding. *Acc Chem Res*. 2008;41(3):442-451.
16. Palmer AG 3rd, Kroenke CD, Loria JP. Nuclear magnetic resonance methods for quantifying microsecond-to-millisecond motions in biological macromolecules. *Methods Enzymol*. 2001;339:204-238.
17. Hoch JC, Baskaran K, Burr H, et al. Biological magnetic resonance data bank. *Nucleic Acids Res*. 2022;51(D1):D368-D376. <https://doi.org/10.1093/nar/gkac1050>
18. Tugarinov V, Kay LE. Methyl groups as probes of structure and dynamics in NMR studies of high-molecular-weight proteins. *Chem-biochem*. 2005;6(9):1567-1577.
19. Haigh CW, Mallion RB. Ring current theories in nuclear magnetic resonance. *Prog Nucl Magn Reson Spectrosc*. 1979;13(4):303-344.
20. Berjanskii MV, Wishart DS. A simple method to predict protein flexibility using secondary chemical shifts. *J Am Chem Soc*. 2005;127(43):14970-14971.
21. Marsh JA, Singh VK, Jia Z, Forman-Kay JD. Sensitivity of secondary structure propensities to sequence differences between  $\alpha$ - and  $\gamma$ -synuclein: Implications for fibrillation. *Protein Sci*. 2006;15(12):2795-2804.
22. Nielsen JT, Mulder FAA. POTENCI: prediction of temperature, neighbor and pH-corrected chemical shifts for intrinsically disordered proteins. *J Biomol NMR*. 2018;70:141-165.
23. Sekhar A, Kay LE. NMR paves the way for atomic level descriptions of sparsely populated, transiently formed biomolecular conformers. *Proc Natl Acad Sci*. 2013;110(32):12867-12874.
24. Reid Alderson T, Kay LE. Unveiling invisible protein states with NMR spectroscopy. *Curr Opin Struct Biol*. 2020;60:39-49.
25. Kuwajima K, Yagi-Utsumi M, Yanaka S, Kato K. DMSO-quenched H/D-exchange 2D NMR spectroscopy and its applications in protein science. *Molecules*. 2022;27(12):3748-8418.
26. Zimm BH, Bragg JK. Theory of the phase transition between helix and random coil in polypeptide chains. *J Chem Phys*. 1959;31:526-535.
27. Seeling J, Schönfeld H-J. Thermal protein unfolding by differential scanning calorimetry and circular dichroism spectroscopy Two-state model versus sequential unfolding. *Q Rev Biophys*. 2016;49:1-24.
28. Shin Y, Qayyum MZ, Pupov D, Eshyuna D, Kulbachinskiy A, Murakami KS. Structural basis of ribosomal RNA transcription regulation. *Nat Commun*. 2021;12:528.
29. Krásný L, Gourse RL. An alternative strategy for bacterial ribosome synthesis: *Bacillus subtilis* rRNA transcription regulation. *EMBO J*. 2004;23:4473-4483.
30. Gauvry E, Mathot A-G, Couvert O, Leguérinel I, Coroller L. Effects of temperature, pH and water activity on the growth and the sporulation abilities of *Bacillus subtilis* BSB1. *Int J Food Microbiol*. 2021;337:108915.
31. Hubin EA, Lilic M, Darst SA, Cambell EA. Structural insights into mycobacteria transcription initiation complex from analysis of X-ray crystal structures. *Nat Commun*. 2017;8:16072.
32. Pletnev P, Pupov D, Pshanichnaya L, et al. Rewiring of growth-dependent transcription regulation by a point mutation in region 1.1 of the house-keeping  $\sigma$  factor. *Nucleic Acids Res*. 2020;48(19):10802-10819.
33. Patel UR, Gautam S, Chatterji D. Validation of omega subunit of RNA polymerase as a functional entity. *Biomolecules*. 2020;10(11):1588.
34. Kerfah R, Plevin MJ, Sounier R, Gans P, Boisbouvier J. Methyl-specific isotopic labeling: a molecular tool box for solution NMR studies of large proteins. *Curr Opin Struct Biol*. 2015;32:113-122.
35. Gans P, Hamelin O, Sounier R, et al. Stereospecific isotopic labeling of methyl groups for NMR spectroscopic studies of high-molecular-weight proteins. *Angew Chem*. 2010;122(11):2002-2006.
36. Lundström P, Teilum K, Carstensen T, et al. Fractional  $^{13}\text{C}$  enrichment of isolated carbons using [ $1\text{-}^{13}\text{C}$ ] or [ $2\text{-}^{13}\text{C}$ ] glucose facilitates the accurate measurement of dynamics at backbone  $\text{C}^\alpha$  and side-chain methyl positions in proteins. *J Biomol NMR*. 2007;38(3):199-212.
37. Patrick Loria J, Rance M, Palmer AG. A relaxation-compensated Carr-Purcell-Meiboom-Gill sequence for characterizing chemical exchange by NMR spectroscopy. *J Am Chem Soc*. 1999;121(10):2331-2332.
38. Yip GNB, Zuiderweg ERP. A phase cycle scheme that significantly suppresses offset-dependent artifacts in the  $\text{R}_2$ -CPMG  $^{15}\text{N}$  relaxation experiment. *J Magn Reson*. 2004;171(1):25-36.
39. Vallurupalli P, Hansen DF, Stollar E, Meirovitch E, Kay LE. Measurement of bond vector orientations in invisible excited states of proteins. *Proc Natl Acad Sci*. 2007;104(47):18473-18477.
40. Hansen MR, Hanson P, Pardi A. Filamentous bacteriophage for aligning RNA, DNA, and proteins for measurement of nuclear magnetic resonance dipolar coupling interactions. *Methods Enzymol*. 2000;317:220-240.
41. Rückert M, Otting G. Alignment of biological macromolecules in novel nonionic liquid crystalline media for NMR experiments. *J Am Chem Soc*. 2000;122(32):7793-7797.
42. Ottiger M, Delaglio F, Bax A. Measurement of J and dipolar couplings from simplified two-dimensional NMR spectra. *J Magn Reson*. 1998;131(2):373-378.
43. Vallurupalli P, Bouvignies G, Kay LE. Studying “invisible” excited protein states in slow exchange with a major state conformation. *J Am Chem Soc*. 2012;134:8148-8161.
44. Kay LE, Bouvignies G, Vallurupalli P. Visualizing side chains of invisible protein conformers by solution NMR. *J Mol Biol*. 2014;426:763-774.
45. Kay LE, Long D, Sekhar A. Triple resonance-based  $^{13}\text{C}^\alpha$  and  $^{13}\text{C}^\beta$  cest experiments for studies of ms timescale dynamics in proteins. *J Biomol NMR*. 2014;60:203-208.
46. Kay LE, Vallurupalli P. Probing slow chemical exchange at carbonyl sites in proteins by chemical exchange saturation transfer NMR spectroscopy. *Angew Chem*. 2013;52:4156-4159.
47. Yuwen T, Bouvignies G, Kay LE. Exploring methods to expedite the recording of CEST datasets using selective pulse excitation. *J Magn Reson*. 2018;292:1-7.
48. Baldwin AJ, Hansen DF, Vallurupalli P, Kay LE. Measurement of methyl axis orientations in invisible, excited states of proteins by relaxation dispersion NMR spectroscopy. *J Am Chem Soc*. 2009;131:11939-11948.
49. Kay LE, Skrynnikov NR, Dahlquist FW. Reconstructing NMR spectra of “invisible” excited protein states using HSQC and HMQC experiments. *J Am Chem Soc*. 2002;124:12352-12360.
50. Delaglio F, Grzesiek S, Vuister GW, Zhu G, Pfeifer J, Bax AD. NMRpipe: a multidimensional spectral processing system based on UNIX pipes. *J Biomol NMR*. 1995;6(3):277-293.
51. Lee W, Tonelli M, Markley JL. NMRFAM-SPARKY: enhanced software for biomolecular NMR spectroscopy. *Bioinformatics*. 2015;31(8):1325-1327.
52. Eaton JW, Bateman D, Hauberg S, Wehbring R. *GNU Octave Version 3.8.1 manual: a high-level interactive language for numerical computations*. CreateSpace Independent Publishing Platform; 2014.
53. Carver JP, Richards RE. A general two-site solution for the chemical exchange produced dependence of  $T_2$  upon the Carr-Purcell pulse separation. *J Magn Reson (1969)*. 1972;6(1):89-105.

54. Sugase K, Konuma T, Lansing JC, Wright PE. Fast and accurate fitting of relaxation dispersion data using the flexible software package GLOVE. *J Biomol NMR*. 2013;56(3):275-283.
55. Chang BY, Doi RH. Overproduction, purification, and characterization of *Bacillus subtilis* RNA polymerase  $\sigma^A$  factor. *J Bacteriol*. 1990;172:3257-3263.
56. Qi Y, Hulett FM. PhoP~P and RNA polymerase  $\sigma^A$  holoenzyme are sufficient for transcription of Pho regulon promoters in *Bacillus subtilis*: PhoP~P activator sites within the coding region stimulate transcription *in vitro*. *Mol Microbiol*. 1998;28:1187-1197.
57. Krásný L, Tišerová H, Jonák J, Rejman D, Šanderová H. The identity of the transcription +1 position is crucial for changes in gene expression in response to amino acid starvation in *Bacillus subtilis*. *Mol Microbiol*. 2008;28:42-54.

## SUPPORTING INFORMATION

Additional supporting information can be found online in the Supporting Information section at the end of this article.

**How to cite this article:** Tužinčin D, Padrta P, Šanderová H, et al. Characterization of a transitionally occupied state and thermal unfolding of domain 1.1 of  $\sigma^A$  factor of RNA polymerase from *Bacillus subtilis*. *Proteins*. 2023;1-12. doi:10.1002/prot.26531